Applied Catalysis B: Environmental 164 (2015) 261–270

Contents lists available at ScienceDirect

Applied Catalysis B: Environmental

journal homepage: www.elsevier.com/locate/apcatb

Promotion of CeO_2–TiO_2 photoactivity by g-C_3N_4: Ultraviolet and visible light elimination of toluene

Mario J. Muñoz-Batista, Marcos Fernández-García*, Anna Kubacka*

Instituto de Catálisis y Petroleoquímica, CSIC, Marie Curie 2, 28049 Madrid, Spain

ARTICLE INFO

Article history:
Received 9 July 2014
Received in revised form
10 September 2014
Accepted 16 September 2014
Available online 28 September 2014

Keywords:
Photo-catalysis
Mineralization
UV
Sunlight
Titania

ABSTRACT

Promotion of a CeO_2–TiO_2 photocatalyst by variable quantities of g-C_3N_4 was essayed with a combination of microemulsion and impregnation preparative methods. The resulting materials were characterized with the help of X-ray diffraction and photoelectron, infrared, UV–visible and photoluminescence spectroscopies and transmission electron microscopy. The photoactivity of the materials in the elimination of toluene was evaluated under UV and sunlight-type illumination conditions and quantitatively analyzed through the calculation of the corresponding quantum yield values. Irrespective of the illumination conditions, maximum activity was observed for the sample promoted with a 1 wt.% of carbon nitride. The characterization study unveiled the interplay between the different components of the ternary system and allowed spotting out the key physico-chemical variables governing photoactivity.

1. Introduction

Photocatalytic ternary systems are relatively scarce [1,2]. The literature accounts for metal–sulphide–oxide or metal–halide–oxide as the most frequently used [1–6]. In such systems the metals like Pt or Ag are typically shuttle components to send or receive charge carriers or to provide effective recombination centers spatially separated from reaction centers. For such reasons, if the system is adequately engineered and optimum phase contact achieved, an improvement in charge carrier lifetime for the overall system and subsequent enhancement of chemical activity is observed. Besides this critical point, the combination of phases may provide different surfaces with high specificity for certain reaction steps. An illustrative example could be the use of a metal surface to handle multielectron reaction steps while hole-related species are frequently handled at semiconductor surfaces such as the titania one, the most active and universal single-phase photocatalyst up to know described [1,2,7].

In this contribution we combine a dominant (by weight percentage) anatase component with two semiconductors of different chemical nature. The first is cerium oxide. The contact between ceria and titania is known to provide rather active materials independently of the excitation wavelength [2,8]. It has been applied for the elimination of organic pollutants through reduction and/or oxidation reactions [9–18] and, very recently, for the inactivation of microorganisms [16,18]. The second is the g-C_3N_4 carbon nitride. Similarly to the previous case, the combination with titania has shown to provide outstanding photo-chemical activity in hydrogen production [19,20] or CO_2 reduction [21], as well as a series of degradation reactions concerning several pollutants such as formaldehyde [22], phenol [23], toluene [24], organic dyes [25–28] as well as the removal of Cr(VI) [25]. As described in the literature for both binary systems, under UV excitation a consistent enhancement of activity can be observed irrespective of the photo-elimination target. This is mostly ascribed to an adequate handling of charge carriers under reaction conditions [8,28]. Under visible light the situation is more complex. Both, ceria and the carbon nitride permit a significant increase of light adsorption in the visible electromagnetic range but their effect in the light-triggered charge carriers is more complex to analyze, being this particularly true in the case of the carbon nitride [19–28].

For such reasons here we will study the influence of growing quantities the g-C_3N_4 component in contact with a previously tested and optimized ceria–titania (CeO_2–TiO_2) binary oxide system [17,18,29]. In such CeO_2–TiO_2 system, maximum enhancement of the photocatalytic activity in toluene photo-degradation is detected in the presence of a 2.5 mol.% of ceria. The use of

* Corresponding authors. Fax: +34 915854760.
E-mail addresses: mfg@icp.csic.es (M. Fernández-García), ak@icp.csic.es, a.kubacka@icp.csic.es (A. Kubacka).

http://dx.doi.org/10.1016/j.apcatb.2014.09.037
0926-3373/

relatively small quantities, always below 10 mol.%, of ceria to enhance photoactivity of titania is a general result of the literature [9–18,29].

With the carbon nitride–ceria–titania ternary materials we carried out the photo-degradation of toluene as it is a typical pollutant present in urban atmospheres which demands highly active photocatalysts for its elimination [30–33]. To provide a rigorous, quantitative analysis of the activity we will present results based on quantum yield calculations under all illumination conditions essayed. The calculation of the quantum yield of the reaction, involves in first place the measurement and modeling of the radiation reached the surface of the material and the fraction effectively used in photo-catalytic steps. Such task typically requires, in first place, the measurement and modeling of the light source emission properties and, subsequently, the light absorption capability of the photocatalysts. The latter takes into account the calculation of the radiative transfer equation by calculating in our case the so-called local superficial rate of photon absorption ($e^{a,s}$) [29,34–37]. On second place, the accurate calculation of the quantum yield requires to take into account the number of charge carriers used for each specific chemical product of the reaction [24].

In addition and with the aim of interpreting the quantum yield results on physico-chemical basis we carried out a multitechnique examination of the materials using X-ray diffraction, photoelectron, and infrared spectroscopies, photoluminescence and ultraviolet spectroscopies and transmission electron microscopy. Applying these tools we would like to interpret the ternary system behavior under UV and visible light illumination conditions. We encountered a single maximum, coincident for all illumination conditions. The work attempted to provide a chemical interpretation of the series behavior as a function of the sample chemical composition.

2. Materials and methods

2.1. Catalyst preparation

Materials were prepared using a microemulsion preparation method using *n*-heptane (Scharlau) as organic media, Triton X-100 (Aldrich) as surfactant and hexanol (Aldrich) as cosurfactant. A TiO_2 reference sample was obtained as a first step using a microemulsion into the aqueous phase and titanium tetraisopropoxide as precursor. In the CeO_2–TiO_2, and CeO_2 reference, cerium nitrate (Alfa Aesar) was introduced in the aqueous phase of a microemulsion. After 30 min of agitation, a stoichiometric quantity of tetramethylammonium-hydroxide (TMAH) to obtain 2.5% of Ce(III) hydroxide was introduced from the aqueous phase of a similar microemulsion. After 5 min, titanium tetraisopropoxide was introduced into the previously resulting microemulsion drop by drop from a mixture with isopropanol (2:3). Water/(Ti + Ce) and water/surfactant molar ratios were, 110 and 18 for all samples respectively [38,39]. The resulting mixture was stirred for 24 h, centrifuged, and the separated solid precursors rinsed with methanol and dried at 110 °C for 12 h. After drying, the solid precursors were subjected to a heating ramp (2 °C min^{-1}) up to 500 °C, maintaining this temperature for 2 h.

The graphitic carbon nitride (g-C_3N_4) was obtained by calcination of melamine (Aldrich) at 580 °C with a heating ramp of 5 °C min^{-1} for 4 h. The incipient wetness impregnation method was used to obtain the g-C_3N_4–CeO_2–TiO_2 ternary composites. For this, the appropriate amount of g-C_3N_4 was suspended into methanol and sonicated for 1 h, deposited on the CeO_2–TiO_2 composite sample and dried at 110 °C for 24 h. Sample names are Ti, CeTi and g for the TiO_2, CeO_2–TiO_2 and g-C_3N_4 references, respectively, and *x* g/CeTi for the composite ones, where *x* is the wt.% (0.5, 1, 2, 4) of g-C_3N_4 with respect to TiO_2. This was confirmed with an error below 5% using ICP-AAS spectrometry.

2.2. Experimental techniques

The Brunauer–Emmett–Teller (BET) surface areas and average pore volumes and sizes were measured by nitrogen physisorption (Micromeritics ASAP 2010). XRD profiles were obtained with a Seifert D-500 diffractometer using Ni-filtered Cu Kα radiation with a 0.02° step and fitted using the Von Dreele approach to the Le Bail method [40]; particle sizes and microstrain were measured with XRD using the Willianson–Hall formalism [41]. UV–vis transmission or diffuse-reflectance spectroscopy experiments were performed with a Shimadzu UV2100 apparatus using, for diffuse experiments, $BaSO_4$ as a reference. TEM analysis of the materials was carried out with a JEOL 2100F TEM/STEM microscope. X-ray energy dispersive spectra (XEDS) analysis was performed in STEM mode, with a probe size ~1 nm, using the INCA *x*-sight (Oxford Instruments) detector. Photoluminescence spectra were measured at room temperature on a Fluorescence Spectrophotometer (Perkin Elmer LS50B). The Fourier transform infrared spectra were taken in a Bruker Vertex 80 FTIR spectrometer sing a MCT detector. XPS data were recorded on 4 mm × 4 mm pellets, 0.5 mm thick, prepared by slightly pressing the powered materials which were outgassed in the prechamber of the instrument at room temperature up to a pressure $<2 \times 10^{-8}$ Torr remove chemisorbed water from their surfaces. The SPECS spectrometer main chamber, working at a pressure $<10^{-9}$ Torr, was equipped with a PHOIBOS 150 multichannel hemispherical electron analyser with a dual X-ray source working with Ag Kα ($h\nu$ = 1486.2 eV) at 120 W, 20 mA using C 1s as energy reference (284.6 eV). Surface chemical compositions were estimated from XP-spectra, by calculating the integral of each peak after subtraction of the "S-shaped" Shirley-type background using the appropriate experimental sensitivity factors and the CASA-XPS (version 2.3.15) software.

2.3. Photo-catalytic experimental details

Gas-phase photo-oxidation of toluene (Panreac, spectroscopic grade) was carried in a continuous flow annular photoreactor out with and using a set-up described elsewhere [29,42,43]. Activity and selectivity for the gas-phase photooxidation were tested in a continuous flow annular photoreactor containing ca. 40 mg of photocatalyst as a thin layer coating on a pyrex tube. The corresponding amount of catalyst was suspended in 1 mL of ethanol, painted on a pyrex tube (cut-off at ca. 290 nm), and dried at RT. The reacting mixture (100 ml/min) was prepared by injecting toluene (≥99%; Aldrich) into a wet (ca. 75% relative humidity) 20 vol.% O_2/N_2 flow before entering to the photoreactor, yielding an organic inlet concentration of ca. 700 ppmv. Under such conditions, the reaction rate shows a zero-order kinetics with respect to the total flow and organic pollutant/oxygen concentrations. After flowing the mixture for 6 h (control test) in the dark, the catalyst was irradiated by four fluorescent daylight lamps (6W, Sylvania F6W/D) with a radiation spectrum simulating sunlight (UV content of 3%); main emission lines at 410, 440, 540, and 580 nm, symmetrically positioned outside the photoreactor. Similar tests were carried out using UV lamps (Sylvania F6WBLT-65; 6 W, maximum at ca. 350 nm). Reaction rates were evaluated (vide supra) under steady-state conditions, typically achieved after ca. 6–10 h from the irradiation starting. No change in activity was detected for all samples within the next 24 h. The concentration of reactants and products was analyzed using an on-line gas chromatograph (Agilent GC 6890) equipped with HP-PLOT-Q/HP-Innowax columns (0.5/0.32 mm I.D. × 30 m) and TCD

Table 1
Band gap and Morphological Properties for the reference and *x* g/CeTi samples.

Sample	Band gap (eV)	BET surface area ($m^2\ g^{-1}$)	Pore volume ($cm^3\ g^{-1}$)	Pore size (nm)
Ti	3.20	91.8	0.123	5.2
CeTi	2.97	105.7	0.112	4.2
0.5 g/CeTi	2.97	101.7	0.109	4.3
1 g/CeTi	2.88	103.1_5	0.110	4.3
2 g/CeTi	2.89	100.1	0.107	4.3
4 g/CeTi	2.86	101.0_5	0.111	4.3
g	2.70	26.8	0.103	15.1

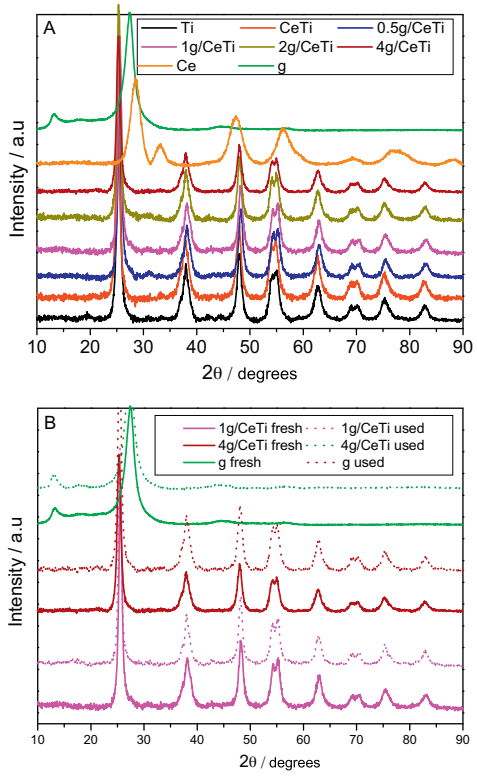

Fig. 1. XRD patterns of *x* g/CeTi samples and reference systems. (A) Fresh samples; (B) comparative of selected samples before and after reaction.

(for CO_2 measurement)/FID (organic measurement) detectors. Carbon balance is above 95% in all experiments.

3. Results and discussion

3.1. Characterization

The physico-chemical characterization of the samples is summarized in Table 1. Starting with the surface area, our TiO_2 reference present a value of ca. $91.8\ m^2\ g^{-1}$. This observable increases by ca. $15\ m^2\ g^{-1}$ in the presence of CeO_2 while the subsequent addition of g-C_3N_4 does not significantly modify the surface area. If compared with the carbon nitride reference we thus observed that the surface area is dominated by the major titania component with a positive effect of CeO_2 and a nearly null of g-C_3N_4. Such situation can be extended to the interpretation of other morphological properties as demonstrated by the pore volume and size reported in Table 1.

The X-ray diffraction patterns of the *x* g/CeTi samples and corresponding single and binary reference systems are shown in Fig. 1. The comparison of the patterns makes obvious the exclusive presence of anatase (JCPDS card 78-2486, corresponding to the $I4_1/amd$ space group). Table 2 lists the data for the anatase primary particle size, strain and cell parameters. In panel B of Fig. 1 we show representative examples of the XRD patterns for samples after reaction. The absence of differences between fresh and used samples and thus similar parameters to those presented in Table 2 can be noticed. We also would like to highlight the fact that XRD (similarly to Raman, see Ref. [17]) does not provide information about the ceria component. The state of ceria is however analyzed with the help of other techniques (see below).

Table 2
XRD-derived parameters for the anatase phase for Ti and CeTi references and *x* g/CeTi samples.

Sample	Size (nm) TiO_2	Microstrain $\langle\xi^2\rangle^{1/2}$ ($\times10^{-3}$) TiO_2	TiO_2 anatase cell parameters (Å)	
			a	*c*
Ti	12.1	2.08	3.789	9.481
CeTi	13.7	1.97	3.794	9.497
0.5 g/CeTi	12.9	1.99	3.792	9.496
1 g/CeTi	13.0	1.97	3.793	9.493
2 g/CeTi	12.9	2.01	3.789	9.489
4 g/CeTi	13.1	1.97	3.790	9.487

Table 3
C1s XPS fitting results for the g reference, 1g-CeTi and 4g-CeTi samples.

Sample	C1s					
	C—C	%	$(C)_3$—N	%	C—N—C	%
g	284.6	10.1	286.2	7.3	287.6	82.6
1g-CeTi	284.6	54.0	286.1	3.4	287.8	42.6
4g-CeTi	284.6	38.4	286.0_5	4.8	287.7	56.8

Table 4
N1s XPS fitting results for the g reference, 1g-CeTi and 4g-CeTi samples.

Sample	N1s							
	Pi-exc.	%	N—H	%	$(C)_3$—N	%	C—N—C	%
g	403.4	5.1	400.6	13.7	399.2	25.7	397.5	55.5
1g-CeTi	403.9	5.4	400.2	12.5	399.1	24.3	398.3	57.8
4g-CeTi	403.6	4.8	400.3	14.1	399.2	23.3	397.7	57.8

In consonance with the morphological properties just described, the anatase properties included in Table 2 change moderately from TiO_2 and CeO_2–TiO_2 samples and only very modestly in the presence of the carbon nitride component. The similar behavior of all structural and morphological parameters of Tables 1 and 2 is, as already mentioned, a consequence of the preparation method (ceria–titania is prepared by a single pot procedure and subsequently modified with the carbon nitride component using a simple impregnation method) and the limited weight/molar content of the non-TiO_2 components in the *x* g/CeTi system. While the CeO_2–TiO_2 system is produced in a single pot procedure, the introduction of the carbon nitride using relatively mild conditions does not affect the CeO_2–TiO_2 counterpart. In particular we note that carbon doping of titania/ceria in the TiO_2 or CeO_2–TiO_2 samples does not occurs as judged by the constancy of the cell parameters reported in Table 2.

To provide information of the minor CeO_2 or g-C_3N_4 components in the catalysts, we carried out a joint XPS and infrared study. Fig. 2 displays representative XPS results for the carbon 1s (C1s) and nitrogen 1s (N1s) experimental and fitting results. A full summary of the fitting is summarized in Table 3 for C1s and Table 4 for N1s. The remaining elements present in the samples were also studied by XPS and results described in Table 5. Such table shows no important differences at the Ce3d, Ti2p, and O1s peaks in the presence/absence of g-C_3N_4 or among *x* g/CeTi samples with respect to the CeTi reference. XPS analysis, the most significant technique providing structural and electronic information of the ceria

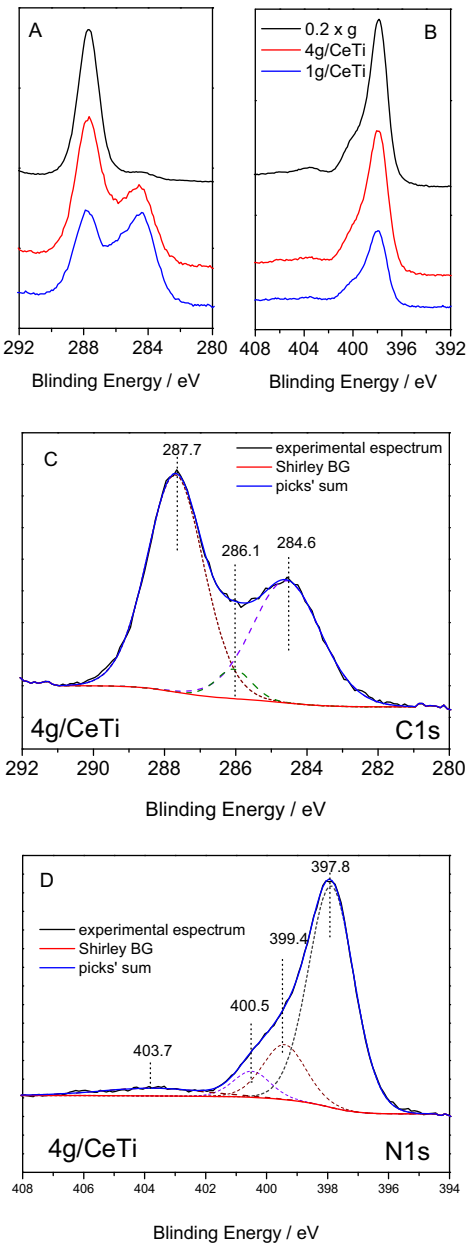

Fig. 2. C1s (A) and N1s (B) XPS spectra for the 1 g/CeTi, 4 g/CeTi and g samples. Representative example of the fitting procedure for the C1s (C) and N1s (D) XPS spectra of the 4 g/CeTi sample.

Table 5
Ce, Ti and O XPS fitting results for the CeTi reference, 1g-CeTi and 4g-CeTi samples.

Sample	Ce3d$_{3/5}$ (u''')	Ti2p$_{3/2}$	O1s
CeTi	916.6	458.3	529.6
1g-CeTi	916.6	458.2	529.4
4g-CeTi	916.6	458.1	529.4

component, indicated the presence of ceria and titania oxides but interface effects produce a rather high Ce(III)/Ce(IV) atomic ratio of ca. 3.2, see Ref. [17] for further details. As mentioned, such situation holds here for all *x* g/CeTi catalysts without relevant differences among them.

Most interesting for our purposes would be the results of the C1s and N1s peaks illustrated in Fig. 2. The fitting results of Fig. 2 (Tables 3 and 4) provide evidence that most important differences are detected in the C1s and more exactly when compared

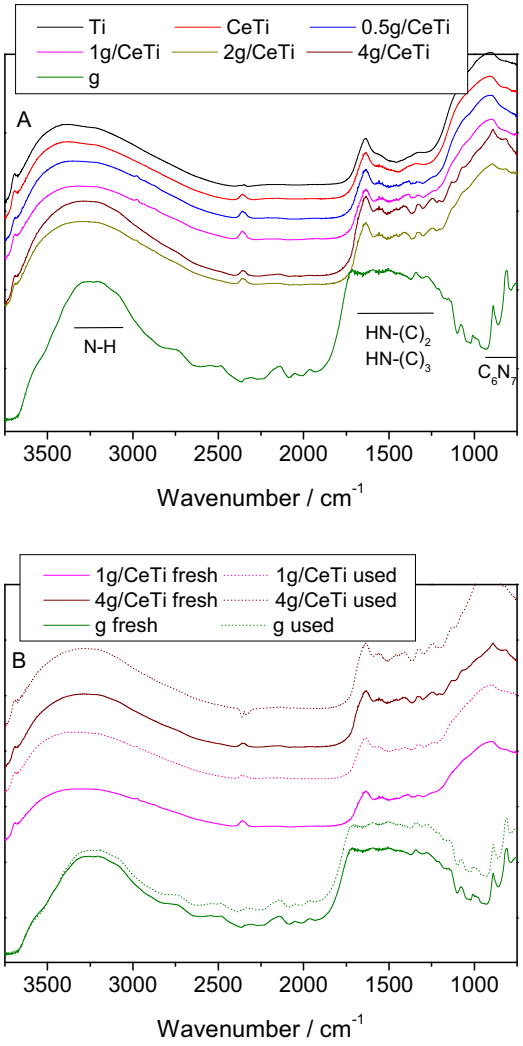

Fig. 3. FTIR spectra of the *x* g/CeTi samples and g reference. (A) Fresh samples; (B) comparative of selected samples before and after reaction.

the g-C_3N_4 reference and the catalysts. Three components were observed at the C1s XPS signal. As previously reported by others in similar systems, the C—C contribution shows the larger variation as a consequence of the different importance of the spurious carbon-containing entities [44,45]. The other contributions exclusively ascribable to carbon nitride structural moieties, e.g. bridging carbons between aromatic moieties (C_3—N) or at the aromatic rings (N—C—N), are also included in Table 3 [20,44,45]. They are essentially constant through the *x* g/CeTi sample series; particularly, no significant differences appear in the binding energy values of both contributions at the samples and/or the g-C_3N_4 reference. This indicates the rather minor differences in terms of the carbon nitride component among the *x* g/CeTi samples. This observation is also sustained by the N1s results reported in Table 4, where the rough constancy of the corresponding contributions is observed in both the binding energy and intensity, particularly in those contributions related to ($C)_3$—N and C—N—C moieties.

Corroboration of the XPS results was achieved using infrared spectroscopy (Fig. 3). In the case of the g-C_3N_4 reference, from high to lower wave numbers we detected the presented of N—H stretching vibration contribution(s) at the 3500–2500 cm^{-1} region. This is related to residual NH_x groups although the presence of adsorbed water molecules may also need to be considered [19,24,46]. After it, in the 1600–1200 cm^{-1} region we can observe several

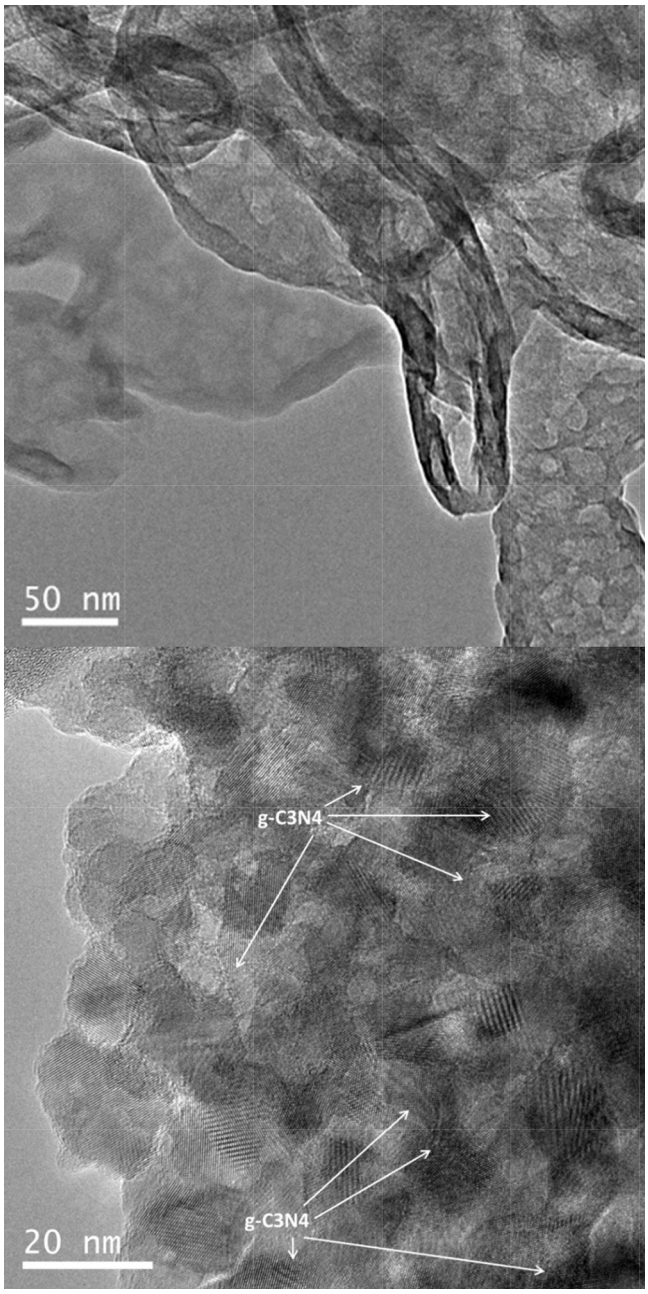

Fig. 4. TEM views of g reference (A) and 4 g/CeTi sample (B).

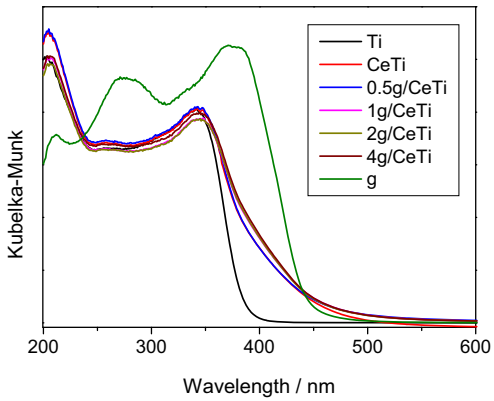

Fig. 5. UV–vis spectra of the *x* g/CeTi samples and reference systems.

contributions mostly associated to N—C stretching modes of heterocycil compounds. Finally, around 850–800 cm^{-1} we note additional contributions coming from the breathing modes of tris-s-triazine (C_6N_7-based) building blocks [45,47,48]. The same contributions can be observed in composite catalysts having a carbon nitride content equal or superior to 1 wt.%. Of course, in some regions, typically water or hydroxyl related ones, they are overlapped with intrinsic titania contributions. The region below ca. 1600 cm^{-1} displays however clear carbon nitride like fingerprints in the composite catalysts. Specifically, in the 1600–800 cm^{-1} region, although some of the bands present differences between the composites and the g-C_3N_4 reference, the constancy of the tris-s-triazine breathing mode frequency indicates that the carbon nitride component maintains its main structural characteristics in the *x* g/CeTi samples, in agreement with the XPS results previously reported. The stability of the main oxidic component was previously tested with XRD and here we use IR for the specific case of the g-C_3N_4 component. After removal of adsorbed species from the materials surface and as it is shown in panel B of Fig. 3, the absence of significant changes in the breathing mode of the tris-s-triazine moiety would indicate the reasonable maintenance of the integrity of the carbon nitride structure during reaction.

To visualize the interaction between the components, a TEM study of the materials is presented in Fig. 4. Fig. 4A micrograph corresponds to the g-C_3N_4 reference while Fig. 4B micrograph concerns the 4 g/CeTi sample as a representative example of a ternary system. The g-C_3N_4 reference displays its characteristic laminar structure. Considering now the 4 g/CeTi sample, in Fig. 4B we can observe the dominant (titania) oxide component. In some regions of this micrograph EDXS indicates the simultaneous presence of C/N (marked with arrows). Thus, the TEM/EDXS combination illustrates the close contact between the carbon nitride and CeO_2–TiO_2 components both at the periphery but also at all parts of the titania–ceria component. Moreover, as the ceria is a minor component in CeO_2–TiO_2, the g-C_3N_4 is expected to be dominantly in contact with titania. In fact, the EDXS study indicates that this is the case as only the Ti signal is correlated with the C/N ones.

The optical properties of the samples were examined using UV–visible spectroscopy. In Fig. 5 we plotted the *x* g/CeTi and corresponding reference systems spectra. The samples present a spectrum profile dominated by the titania component, displaying the characteristic intensity decay for a band gap energy of ca. 3.2 eV (Table 1). The presence of CeO_2 in the CeTi reference slightly decreases (ca. 0.23 eV) the band gap and modifies the spectrum shape in the visible region (Fig. 5). The effect at the band gap energy is mostly attributable to a quantum size effect at the anatase phase [49] due to the complete absence of doping effects [17,18]. This quantum size effect would be in turn related to surface effects exerted by the species present at the anatase surface as other contributions concerning size/shape/morphology changes (with respect to the bare titania reference sample) would be rather modest according to Tables 1 and 2. The subsequent addition of the g-C_3N_4 component does not alter significantly light absorption properties and ban gap energy. Rather modest changes of ca. 0.1 eV are thus presented in Table 1. In spite of the well-documented g-C_3N_4 light absorption capability in the visible region [24,45], its effect on the estimated band gap of the *x* g/CeTi catalysts is unnoticeable. The results would indicate that the absorption properties at the visible region are dominated by the CeO_2 component but with a non-negligible contribution (mainly visible in Fig. 5 around 400 and 500 nm) from the carbon nitride component. Finally, we note that the band gap calculations in used samples (result not shown) only display variation within experimental error (ca. 0.05 eV), indicating the stability of the *x* g/CeTi samples under reaction conditions. This agrees with the results obtained previously with other

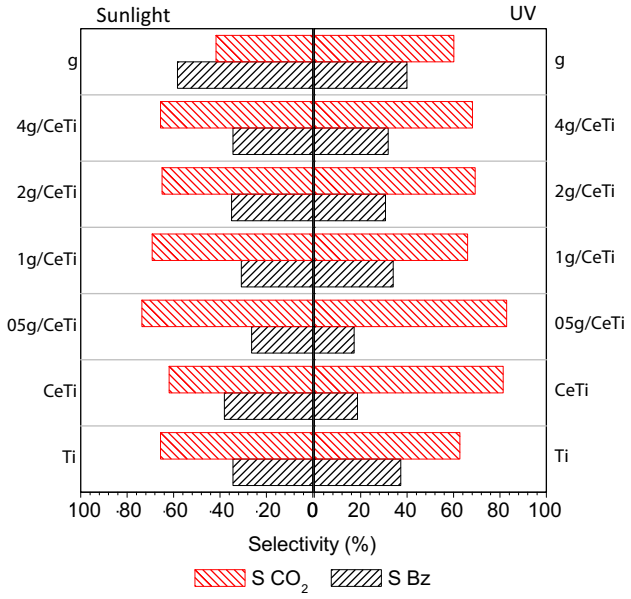

Fig. 6. Selectivity to CO_2 and Benzaldehyde for reference and *x* g/CeTi samples.

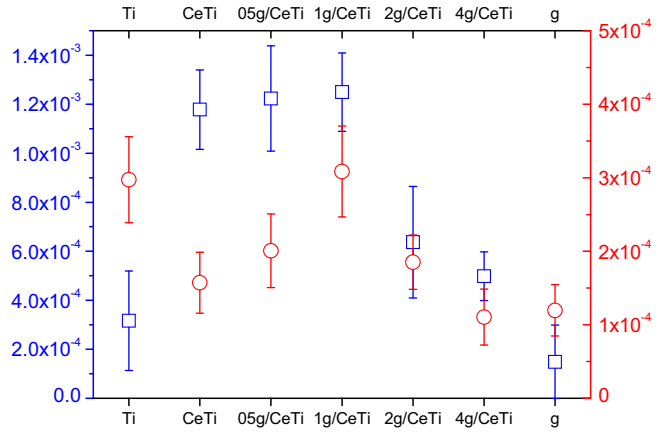

Fig. 7. Quantum yield of the *x* g/CeTi samples under UV (blue square) and sunlight-type (red circle) illumination.

spectroscopies and reinforces the idea that the reaction does not strongly modify the *x* g/CeTi catalysts.

3.2. Photoactivity

The photochemical properties as measured by the reaction rate are reported in Table 6 together with the average value of the local rate of photon absorption at the sample surfaces. The full calculation of the $e^{a,s}$ is detailed in Appendices A and Bsection and requires calculation on a cylindrical geometry and thus two independent geometrical variables. The results under UV and sunlight-type illumination conditions as presented in Figs. A1 and A2. These figures indicates the same geometrical behavior and thus differences between samples can be represented by a single number, the average value of $e^{a,s}$. Quantum yield calculations require the $e^{a,s}$ calculation as well as the measurement of the selectivity of the reaction. In the case of toluene photo-oxidation, only benzaldehyde and CO_2 are observed as reaction products [17,18,24,42,50,51]. The production of such chemical species indicates, according to the literature, the use of 1 and 4 hole-related species for benzaldehyde and CO_2, respectively [17,18,29,50,51]. The ratio between the number of charge species used to produce these two chemical molecules is in any case the important parameter to obtain an accurate measurement of the quantum yield behavior throughout the sample series. Selectivity data for *x* g/CeTi samples and reference systems is presented in Fig. 6.

The results of the quantum yield calculation for all illumination conditions tested in this work are displayed in Fig. 7. In the case of UV light, the addition of ceria seems to have the highest impact in the quantum yield, with a relatively small effect of the carbon nitride component which, however, reaches the optimum for a 1 wt.%. To such maximum contribute mild effects from both the minute change in the local rate of absorption and, of more importance, the change of selectivity (Table 6 and Fig. 6). In this case and as mentioned, these two variables show only modest changes trough the series. For the sunlight-type illumination conditions the strong absorption properties of ceria in the visible electromagnetic region are in the origin of a more important decrease of the quantum yield (Table 6). Note that the effect of selectivity is rather modest as compared with the Ti reference (Fig. 6). When the g-C_3N_4 component is present at the sample, we see an increase in the quantum yield values with moderate effects coming from both the rate of absorption and selectivity (Table 6 and Fig. 6). As previously observed for UV illumination, Fig. 7 displays a maximum through the *x* g/CeTi sample series for the same 1 g/CeTi sample under all illumination conditions tested in this work.

From Fig. 7 it is noticeable the fact that an enhancement of the quantum efficiency of the titania component would occur in the presence of the g-C_3N_4 material. An enhancement of photoactivity of titania by the carbon nitride has been previously shown by many authors [20,24,44,45,47]. Moreover, when measured quantitatively using quantum (or true) yield calculations and taking into account both light absorption and chemical (e.g. activity and selectivity) properties of the samples, such enhancement is observed in all illumination conditions here tested [24]. The maximum occurs roughly for the same concentration of the g-C_3N_4 component here observed, and results indicate that this has complex roots in several photo-physical events characteristic of the binary catalyst and not present in the single reference systems [24]. Thus, the intimate interaction between the components would play a crucial role in the photo-elimination of toluene.

The strong ceria absorption properties in the visible ranges make less obvious the effects taking place in the case of sunlight-type excitation for the CeO_2–TiO_2 catalyst. While the quantum yield suffers a strong increase in the presence of the g-C_3N_4 component, this is just enough to provide a quantum yield value slightly higher than the titania reference. This is a relative paradox but the above discussion makes obvious that the source of that differential behavior lies in the CeO_2 optical properties. The increase in photon absorption in the ternary system is barely balanced with the corresponding enhancement of photo-chemical activity if measured with respect to the Ti reference. In any case, as detailed in Table 6, higher values of the quantum yield are observed for 1 g/CeTi with respect to all Ti, CeTi and g-C_3N_4 reference systems studied.

3.3. Photoluminescence

To interpret in more detailed bases the physical origin of the *x* g/CeTi samples photocatalytic behavior, we carried out photoluminescence experiment under UV and visible light excitation. The corresponding experimental results are presented in the two first panels (A/B) of Fig. 8. UV excitation at 280 nm allows to scan all potential de-excitation channels of the titania, the main component of the *x* g/CeTi materials. Above 2.0 eV the photoluminescence titania samples display the presence of two or three peaks [52–54]. Additional, low energy peaks are less important to generate photo-chemistry and always related to the presence

Table 6
Reaction rates, local superficial rate of photon absorption and quantum efficiencies of the samples under UV and Sunlight-type irradiations.

Sample	UV			Sunlight		
	Reaction rate (mol s^{-1} m^{-1})	$\langle e^{a,s} \rangle$ (einstein cm^{-2} s^{-1})	Quantum efficiency (%)	Reaction rate (mol s^{-1} m^{-1})	$\langle e^{a,s} \rangle$ (einstein cm^{-2} s^{-1})	Quantum efficiency (%)
Ti	1.69×10^{-10}	1.00×10^{-8}	3.2×10^{-4}	1.50×10^{-10}	9.94×10^{-9}	3.0×10^{-4}
CeTi	4.68×10^{-10}	1.02×10^{-8}	11.8×10^{-4}	1.95×10^{-10}	2.31×10^{-8}	1.6×10^{-4}
0.5 g/CeTi	4.69×10^{-10}	1.01×10^{-8}	12.2×10^{-4}	2.11×10^{-10}	2.35×10^{-8}	2.0×10^{-4}
1 g/CeTi	6.37×10^{-10}	1.00×10^{-8}	12.5×10^{-4}	3.52×10^{-10}	2.37×10^{-8}	3.1×10^{-4}
2 g/CeTi	3.09×10^{-10}	1.00×10^{-8}	6.4×10^{-4}	2.26×10^{-10}	2.38×10^{-8}	$1.8_5 \times 10^{-4}$
4 g/CeTi	2.45×10^{-10}	1.00×10^{-8}	5.0×10^{-4}	1.36×10^{-10}	2.40×10^{-8}	1.9×10^{-4}
g	1.49×10^{-10}	1.82×10^{-8}	1.5×10^{-4}	1.55×10^{-10}	1.02×10^{-8}	1.2×10^{-4}

of defective Ti (interstitial or lattice) states [55]. The peaks about 2.0 eV can be grouped in two types of transitions corresponding to high-energy (sometimes called green) and low energy (red) de-excitation channels (see inset in Fig. 8A). Although we lack a definitive interpretation of the photoluminescence spectra of anatase materials, the first transition mostly probes de-excitation of excited electrons in localized (typically oxygen-related) states that annihilates with trap-related holes while the second probes the de-excitation of electron localized states with holes at the valence band [52–54].

For a better visualization of details, the photoluminescence spectra of the *x* g/CeTi samples are compared with the corresponding to a physical mixture of their g-C_3N_4 and CeTi components (panels C and D in Fig. 8). Under UV and visible light excitation, in addition to an obvious increase of photoluminescence intensity with the content of the g-C_3N_4 component, we observed the presence of a dominant peak at ca. 2.55/2.45 eV under UV/visible excitation. Such peak contains an important contribution from the carbon nitride (see the corresponding g-C_3N_4 spectra in Fig. 8A and B). The comparison of the sample spectra and the corresponding physical mixtures gives important clues to interpret photoactivity. The real samples show rather similar signals to the physical mixtures up to the 1 g/CeTi case and lower intensity for samples having higher contents of the carbon nitride. This occurs for all illumination conditions tested. This means that the interaction between the carbon nitride and titania seems to be most

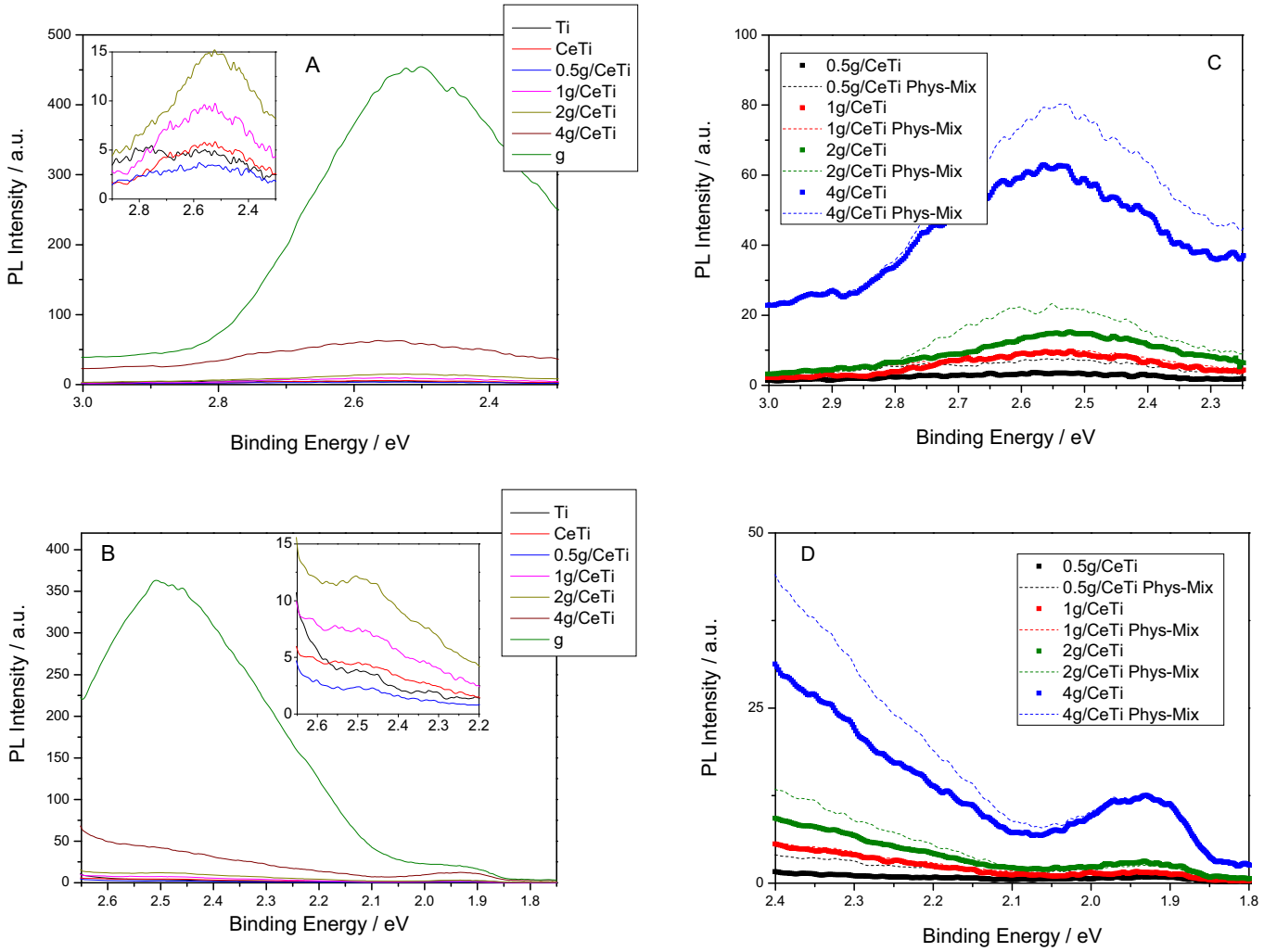

Fig. 8. Photoluminescence spectra of the *x* g/CeTi samples. (A) λ_{ext} = 280 nm. (B) λ_{ext} = 420 nm. PL spectra for composite samples and corresponding physical mixtures under 280 nm (C) and 420 (D) excitation.

effective in terms of decreasing charge recombination as the carbon nitride content grows. This indicates a positive effect on charge carrier recombination, irrespective of the light wavelength. The photo-physical behavior would thus indicate a positive effect of the contact which cannot correlate with the quantum yield above the 1 g/CeTi samples. This would indicate the existence of an additional factor affecting photo-oxidation of toluene. Likely, this corresponds to a masking effect of the carbon nitride. While the local surface rate of photon absorption has a moderate variation through the *x* g/CeTi series ($0.5 \leq x \leq 4$), always below 2.1%, the masking effect originated by the titania surface shadowing originates a significantly larger loss in light to chemical transformation for samples with carbon nitride content above 1 wt.%.

4. Conclusions

In this work a CeO_2–TiO_2 photocatalyst was impregnating with growing quantities of g-C_3N_4 from 0.5 to 4 wt.% using a simple impregnation method. Physico-chemical characterization, particularly TEM, indicates that the g-C_3N_4 component maintains its main structural/electronic properties but, importantly, gets in close contact with the main titania component. Reasonable stability of the *x* g/CeTi system components in terms of main structural/electronic characteristics was also demonstrated using a combination of characterization techniques.

The contact of the carbon nitride and titania alters the photocatalytic behavior of the CeO_2–TiO_2 material in all illumination conditions tested. Full calculation of the quantum yield allows the comparison of toluene degradation activity in the sample series on quantitative basis. A single maximum for the sample with a 1 wt.% of the carbon nitride component was detected for all illumination conditions, i.e. under UV and sunlight-type light. The photoluminescence study strongly indicates that the interaction of the carbon nitride and the ceria–titania component improves charge separation in all conditions essayed and that the maximum achieved for the 1 g/CeTi sample could be the result of a trade-off between the positive effect on charge recombination and a negative coming from a shadowing effect of the carbon nitride on the active titania surface.

Acknowledgements

A. Kubacka and M.J. Muñoz-Batista thank MINECO for support thought, respectively, the postdoctoral "Ramón y Cajal" and predoctoral FPI programs. Financial support by MINECO is also acknowledged (projects CTQ2010-14872/BQU and PRPPRI-PIBJP-2011-0914).

Appendix A. Calculation of quantum efficiency

The quantum efficiency (*Q.E.*) under UV and sunlight irradiation can be determined from the reaction rate and the superficial rate of photon absorption according to Eq. (A1).

$$Q.E.\% = \frac{\text{reaction rate}\ \ (\text{mol m}^{-2}\,\text{s}^{-1})}{\text{photon rate}\ \ (\text{einstein m}^{-2}\,\text{s}^{-1})} \times 100 \qquad \text{(A1)}$$

To evaluate the denominator of this equation, we first evaluate the local net superficial rate of photon absorption ($e^{a,s}$) of the samples (details in Appendix B). Besides, it is necessary to consider the selectivity of the reaction (Eq. (A2)) as two different molecules are obtained in the toluene photo-oxidation reaction. This correction factor (γ) accounts for the number of charge carrier species (and

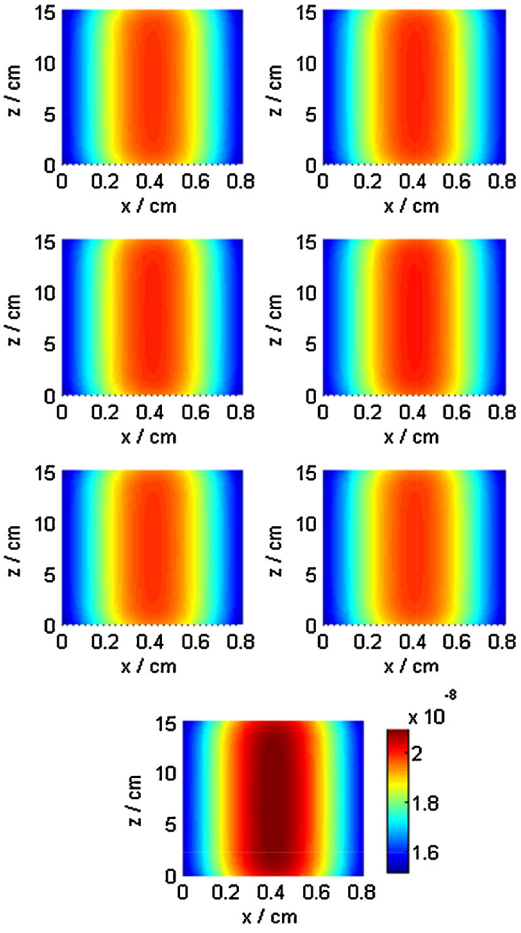

Fig. A1. Local rate of photon absorption (einstein cm^{-2} s^{-1}) under UV irradiation. From top to bottom: Ti, CeTi, 0.5 g/CeTi, 1 g/CeTi, 2 g/CeTi, 4 g/CeTi and g-C_3N_4.

in turn photons) necessary to produce one molecule of a specific product and requires the measurement of the reaction selectivity.

$$\gamma_{TOL} = \sum_i n_i S_i \qquad \text{(A2)}$$

where *i* runs over all products of the reaction, S_i is the fractional selectivity to product *i*, and n_i is the inverse of number of charge carrier species required to obtain the specific *i* product.

Appendix B. Calculation of the $e^{a,s}$ coefficient

In order to compute the UV and sunlight radiation field we adopted the three-dimensional source with superficial emission model and the ray-tracing computational method (see Ref. [29] for details). The spectral local superficial rate of photon absorption at each point on the reactor catalytic (x, y, z) surface is given by Eq. (A3) and are presented in Figs. A1 (UV) and A2 (sunlight-type).

$$e^{a,s}(x,y,z) = \sum_{L=1}^{L=4}\sum_{\lambda}\int_{\varphi_{min}}^{\varphi_{max}}\int_{\theta_{min}}^{\theta_{max}} I_{\lambda,L} \times \exp\left(-\frac{K_{\lambda,g}e_g}{\cos\ \beta}\right) \times \left[1-\exp\left(-\frac{K_{\lambda,s}e_s}{\cos\ \beta}\right)\right]\sin^2\varphi\left[\left(\frac{X_s-X_L}{R}\right)\cos\ \theta+\left(\frac{Y_s}{R}\right)\sin\ \theta\right]d\varphi d\theta + \sum_{L=1}^{L=4}\sum_{\lambda}\int_{\varphi_{min}}^{\varphi_{max}}\int_{\theta_{min}}^{\theta_{max}} I_{\lambda,L} \times \exp\left(-\frac{2K_{\lambda,g}e_g - K_{\lambda,s}e_s}{\cos\ \beta}\right) \times \left[1-\exp\left(-\frac{K_{\lambda,s}e_s}{\cos\ \beta}\right)\right]\sin^2\varphi\left[\left(\frac{X_s-X_L}{R}\right)\cos\ \theta+\left(\frac{Y_s}{R}\right)\sin\ \theta\right]d\varphi d\theta \qquad \text{(A3)}$$

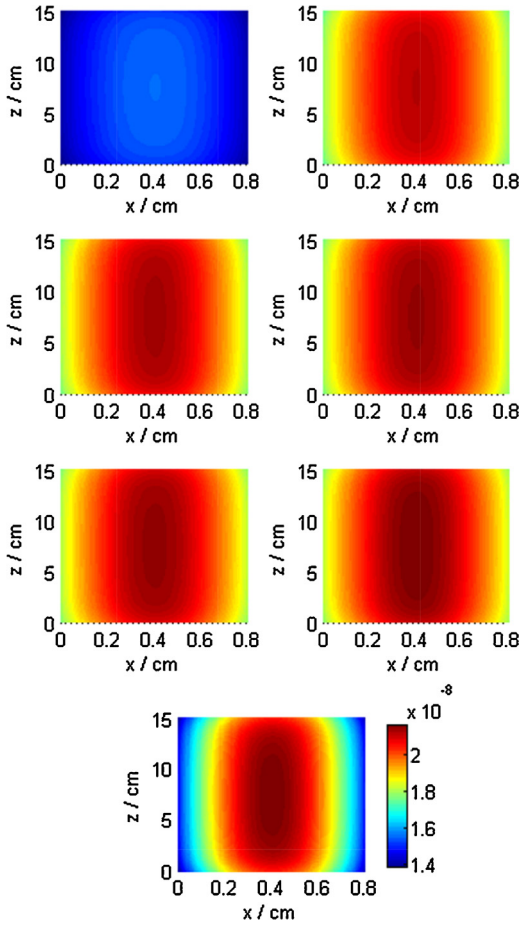

Fig. A2. Local rate of photon absorption (einstein $cm^{-2}\,s^{-1}$) under Sunlight-type irradiation. From top to bottom: Ti, CeTi, 0.5 g/CeTi, 1 g/CeTi, 2 g/CeTi, 4 g/CeTi and g-C_3N_4.

The integration limits for the spherical coordinates φ and θ can be evaluated by the following equations.

$$\varphi_{\min} = \tan^{-1}\left(\frac{X_L - X_s}{Y_L}\right) - \sin^{-1}\left(\frac{R_L}{(X_L - X_s)^2 + (Y_L)^2}\right) \quad \text{(A4)}$$

$$\varphi_{\max} = \tan^{-1}\left(\frac{X_L - X_s}{Y_L}\right) + \sin^{-1}\left(\frac{R_L}{(X_L - X_s)^2 +)(Y_L)^2}\right) \quad \text{(A5)}$$

$$\theta_{min}(\varphi) = cos^{-1}\frac{-Z_s}{(X_{Lm}(\varphi) - X_s)^2 + Y_{Lm}(\varphi)^2 + {Z_s}^2} \quad \text{(A6)}$$

$$\theta_{\max}(\varphi) = \cos^{-1}\frac{Z_L - Z_s}{(X_{Lm}(\varphi) - X_s)^2 + Y_{Lm}(\varphi)^2 + {Z_s}^2} \quad \text{(A7)}$$

where

$$X_{Lm}(\varphi) = X_L + (X_s - Y_L)\cos\varphi^2 + (Y_L)(\cos\varphi\,\mathrm{sen}\,\varphi) - \mathrm{sen}\,\varphi\sqrt{({R_L}^2 - (Y_L\ \mathrm{sen}\,\varphi + (X_s - X_L)cos\,\varphi)^2)} \quad \text{(A8)}$$

$$Y_{Lm}(\varphi) = (Y_L)\cos\varphi^2 - (X_s - X_L)(\cos\varphi\,\mathrm{sen}\,\varphi) - \cos\varphi\sqrt{({R_L}^2 - (Y_L\ \mathrm{sen}\,\varphi + (X_s - X_L)\cos\varphi)^2)} \quad \text{(A9)}$$

I is the radiation intensity and K and e are the equilibrium adsorption constant and thickness (values of $K_{\lambda,g}e_g$ (glass) and $K_{\lambda,s}e_s$ (for each sample), were determined from spectral transmittance measurements), respectively. R is the inner radius reactor annulus, β is the angle between the ray trajectory and the film outwardly directed normal and λ denotes dependency on wavelength. L, s, g refers to lamp, sample and glass, respectively.

References

[1] L. Jing, W. Zhou, G. Tian, H. Fu, Chem. Soc. Rev. 42 (2013) 9509–9549.
[2] A. Kubacka, G. Colón, M. Fernández-García, Chem. Rev. 112 (2012) 1555–1614.
[3] J. Liu, J.Z. Zhang, Coord. Chem. Rev. 253 (2009) 3015–3041.
[4] H.J. Yun, H. Lee, N.D. Kim, D.M. Lee, S. Yu, J. Yi, ACS Nano 5 (2011) 4084–4090.
[5] P.V. Kamat, J. Phys. Chem. Lett. 3 (2012) 663–672.
[6] J. Hou, Z. Wang, C. Yang, W. Zhou, S. Jico, H. Zhu, J. Phys. Chem. C 117 (2013) 5131–5141.
[7] Z. Wang, Y. Liu, B. Huang, Y. Dai, Z. Lou, G. Wang, X. Xhang, X. Qin, Phys. Chem. Chem. Phys. 16 (2014) 2758–2774.
[8] M. Zou, Y. Kong, J. Wang, Q. Wang, Z. Wang, B. Wang, P. Fan, Spectrochim. Acta A 101 (2013) 82–90.
[9] S. Parasupree, Y. Suzuki, S. Prisa-Art, S. Yoshikawa, J. Solid State Chem. 178 (2005) 128–134.
[10] T. Tong, J. Zhang, B. Tian, F. Chen, D. He, M. Anpo, J. Colloid Interface Sci. 315 (2007) 382–388.
[11] G. Li, D. Zhang, Y.C. Yu, Phys. Chem. Chem. Phys. 11 (2009) 3775–3782.
[12] V. Stengl, S. Bakardejieva, N. Murafa, Mater. Chem. Phys. 114 (2009) 217–226.
[13] H. Liu, M. Wang, Y. Wang, Y. Liang, W. Cao, Y. Su, J. Photochem. Photobiol. A 223 (2011) 157–162.
[14] Y. Wang, B. Li, C. Zhang, L. Cui, S. Kang, X. Li, L. Zhou, Appl. Catal. B 130–131 (2013) 277–284.
[15] Y. Liu, P. Fang, Y. Cheng, Y. Gao, F. Chen, Z. Liu, Y. Dai, Chem. Eng. J. 219 (2013) 478–485.
[16] C. Karunakaran, P. Gomathisankar, ACS Sustain. Chem. Eng. 1 (2013) 1555–1563.
[17] M.J. Muñoz-Batista, M.N. Gómez-Cerezo, A. Kubacka, D. Tudela, M. Fernández-García, ACS Catal. 4 (2014) 63–72.
[18] M.J. Muñoz-Batista, M. Ferrer, M. Fernández-García, A. Kubacka, Appl. Catal. B 154–155 (2014) 350–359.
[19] H. Yan, H. Yang, J. Alloys Compd. 509 (2011) L26–L29.
[20] S. Obregón, G. Colón, Appl. Catal. B 144 (2014) 775–783.
[21] S. Zhou, Y. Liu, J. Li, Y. Wang, G. Jiang, Z. Zhao, D. Wang, A. Duan, J. Liu, Y. Wen, Appl. Catal. B 158–159 (2014) 20–29.
[22] J. Yu, S. Wang, J. Low, W. Xiao, Phys. Chem. Chem. Phys. 15 (2013) 16883–16889.
[23] C. Miranda, H. Mansilla, J. Yáñez, S. Obergón, G. Colón, J. Photochem. Photobiol. A 253 (2013) 16–24.
[24] M.J. Muñoz-Batista, A. Kubacka, M. Fernández-García, Catal. Sci. Technol. 4 (2014) 2006–2015.
[25] K. Shidharan, E. Jang, T.J. Park, Appl. Catal. B 142–143 (2013) 718–723.
[26] X.-J. Wang, W.-Y. Yang, F.-T. Li, Y.-B. Xue, R.-H. Liu, Y.-J. Llao, Ind. Eng. Chem. Res. 52 (2013) 17140–17146.
[27] N. Boohprokov, N. Wetchakon, D. Waxler, B. Inceesungrom, J. Colloid Interface Sci. 417 (2014) 402–409.
[28] L. Zhang, D. Jing, X. She, H. Liu, D. Yang, Y. Lu, J. Li, Z. Zheng, L. Gou, J. Mater. Chem. A 2 (2014) 2071–2077.
[29] M.J. Muñoz-Batista, A. Kubacka, M.N. Gómez-Cerezo, D. Tudela, M. Fernández-García, Appl. Catal. B 140–141 (2013) 626–635.
[30] J. Mo, Y. Zhang, Q. Xu, Y. Zhu, J.J. Lamson, R. Zhao, Appl. Catal. B 89 (2009) 570–576.
[31] A. Kubacka, G. Colón, M. Fernández-García, Catal. Today 143 (2009) 286–292.
[32] Y. Luo, W.S. Tan, H.O. Seo, K.-D. Kim, M.J. Kim, N.K. Dey, Y.D. Kim, K.H. Choi, D.C. Lim, Catal. Lett. 130 (2010) 76–81.
[33] A. Kubacka, M.J. Muñoz-Batista, R. Rachwalik, B. Bachiller-Baeza, M. Fernández-García, J. Catal. 309 (2014) 428–438.
[34] G.E. Imoberdorf, A.E. Cassano, O.M. Alfano, H.A. Irazoqui, AIChE J. 52 (2006) 1814–1821.
[35] L. Zhang, W.A. Anderson, Chem. Eng. J. 62 (2010) 1513–1519.
[36] Q.L. Yu, M.M. Ballari, H.J.H. Brouwers, Appl. Catal. B 99 (2010) 58–65.
[37] A.L. Zazueta, H. Destallaits, G.L. Puma, Chem. Eng. J. 217 (2013) 475–482.
[38] P.G. De Gennes, C. Taupin, J. Phys. Chem. 86 (1982) 2294–2303.
[39] M. Fernández-García, X. Wang, C. Belver, J.C. Hanson, J.A. Rodriguez, J. Phys. Chem. C 111 (2007) 674–682.
[40] A. Le Bail, H. Duroy, J.L. Forquet, Mater. Res. Bull. 23 (1988) 447–452.
[41] G.K. Williamson, W.H. Hall, Acta Metall. 1 (1953) 22–31.
[42] A. Fuerte, M.D. Hernández-Alonso, A.J. Maira, A. Martínez-Arias, M. Fernández-García, J.C. Conesa, J. Soria, G. Munuera, Chem. Commun. (2001) 2718–2720.
[43] A. Kubacka, M. Fernández-García, G. Colón, J. Catal. 254 (2008) 272–284.
[44] J. Yu, S. Wang, J. Low, W. Xiao, Phys. Chem. Chem. Phys. 11 (2013) 16883–16890.
[45] G. Dong, Y. Xhang, Q. Pan, J. Qui, J. Phtochem. Photobiol. C 20 (2014) 33–50.
[46] G. Colón, M.C. Hidalgo, J.A. Navío, A. Kubacka, M. Fernández-García, Appl. Catal. B 90 (2009) 633–641.
[47] J.S. Zhang, J.H. Sun, K. Maeda, K. Domen, P. Liu, M. Antonietti, X.Z. Fu, X.C. Wang, Energy Environ. Sci. 4 (2011) 675–678.
[48] M. Xiong, L. Chen, Q. Yuan, J. He, S.-L. Luo, C.T. Au, S.-F. Yin, Dalton Trans. 43 (2014) 8331–8337.
[49] M. Fernández-García, A. Martínez-Arias, J.C. Hanson, J.A. Rodríguez, Chem. Rev. 104 (2004) 4063–4105.

[50] J. Mo, Y. Zhang, Q. Xu, Y. Zhu, J.J. Lamson, R. Zhao, Appl. Catal. B 89 (2009) 570–577.
[51] Y. Feng, L. Li, M. Ge, C. Gou, J. Wang, L. Liu, ACS Appl. Mater. Interfaces 2 (2010) 3134–3142.
[52] T. Tachikawa, T. Majima, J. Am. Chem. Soc. 131 (131) (2009) 8485–8487.
[53] X. Wang, Z. Feng, J. Shi, G. Jia, S. Shen, J. Zhou, C. Li, Phys. Chem. Chem. Phys. 12 (2010) 7083–7089.
[54] C.C. Mercado, Z. Seeley, A. Bandyopadhyay, S. Bose, J.L. McHale, ACS Appl. Mater. Interfaces 3 (2011) 228–235.
[55] E. Finnazi, C.D. Valentin, G. Pacchioni, J. Phys. Chem. C 113 (2009) 3382–3391.